Environmental Science Processes & Impacts

ROYAL SOCIETY OF CHEMISTRY

PAPER

View Article Online
View Journal | View Issue





Cite this: *Environ. Sci.: Processes Impacts*, 2024, **26**, 2177

# Experimental and theoretical investigation of benzothiazole oxidation by OH in air and the role of $O_2$†

Natalia V. Karimova, [a] Weihong Wang, [a] R. Benny Gerber *[ab] and Barbara J. Finlayson-Pitts *[a]

Benzothiazole (BTH) and its derivatives are amongst a group of emerging contaminants that are widely distributed in the environment due to their extensive use in many different consumer products. In air, reaction with the hydroxyl radical (OH) is expected to be a major loss process for BTH in the gas phase, but the kinetics and mechanisms are unknown. Here, we report a combination of experiments and theory to determine both the rate constant and products of the reaction of OH with the smallest member of the series, benzothiazole, in the gas phase. The mechanism first involves an attack by OH on BTH to produce several OHBTH intermediates. This is followed by $O_2$ reactions with OHBTH, leading to several stable products successfully predicted by theory. Relative rate studies at 1 atm in air and 298 K using benzene as a reference gave a rate constant for the BTH + OH reaction of $2.1 \pm 0.1 \times 10^{-12}$ ($1\sigma$) $cm^3$ per molecule per s, which translates to a lifetime in air of 5.5 days at $1 \times 10^6$ OH $cm^{-3}$. Four hydroxybenzothiazole products reflecting attack on different carbon atoms of the benzene ring were measured (*n*-OHBTH, where $n = 4, 5, 6, 7$), with the relative product yields well predicted by the calculated formation energies of the pre-reaction OH···BTH complex. Attack of OH on the –CH of the thiazole ring leads to the formation of 2-OHBTH, representing a smaller fraction of the overall reaction, and is shown to proceed through a more complex mechanism than attack on the benzene ring. A theoretical approach to predicting chromatographic retention times of the products based on solvation free energies ($\Delta G_{solv}$) was successful for most of the products. These studies illustrate how the powerful combination of experiment and theory can be used to predict products of atmospheric oxidation of emerging contaminants and ultimately used to assess their impacts on the environment.

Received 31st July 2024
Accepted 16th October 2024

DOI: 10.1039/d4em00461b

rsc.li/espi

### Environmental significance

Benzothiazole (BTH) and its derivatives (d-BTH) are prevalent in consumer products such as automobile tires, artificial turf, herbicides and fungicides, leading to widespread environmental distribution in surface waters, soil, and urban runoff. These compounds pose significant risks to both human and aquatic health due to their presence in various environmental media and their ability to bioaccumulate. The smallest member of this group, benzothiazole, is sufficiently volatile that it is found in the gas phase as well as in airborne particles. Our study addresses the critical gap in knowledge regarding the gas phase degradation of BTH in the atmosphere, providing essential insights into its environmental fate and guiding future mitigation strategies.

## 1 Introduction

A class of compounds known as benzothiazoles have widespread use[1] in many different rubber products such as automobile tires and crumb rubber products[2–5] made from tires, as well as in plastics, antifreeze, herbicides and algicides, tobacco[6] and textiles.[7] As a result, they are found widely distributed in the environment,[1] as indicated by their detection in human breath[8] as well as urine.[9,10]

The smallest member of this group is benzothiazole (BTH):

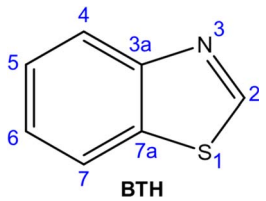

BTH

Common derivatives of BTH are substituted at the 2-position, *e.g.* with an –OH, $–NH_2$, –SH or $–CH_3$ group. With the

[a]*Department of Chemistry, University of California Irvine, CA 92697, USA. E-mail: bgerber@uci.edu; bjfinlay@uci.edu*

[b]*The Institute of Chemistry and Fritz Haber Research Center, The Hebrew University of Jerusalem, 91904 Jerusalem, Israel*

† Electronic supplementary information (ESI) available. See DOI: https://doi.org/10.1039/d4em00461b

exception of the methyl-substituted compound, these derivatives have much lower vapor pressures than BTH (0.07 torr at 25 °C)[1] and hence tend to be found in condensed phases in the environment. As summarized in a review by Liao *et al.*,[1] a variety of toxic effects have been observed for BTH compounds, including genotoxicity and cytotoxicity from *in vitro* studies, and dermatitis, allergic reactions and thyroid hormone-related effects from *in vivo* studies.

Benzothiazole has been detected both indoors and outdoors in particles[11–15] and as well as in the gas phase.[4,11] In a study in Albany, New York, Kannan and coworkers[11] measured BTH and some of its derivatives in particles and the gas phase in automobiles, homes, offices, labs, garages, public places and barbershops. The highest concentrations of BTH were found in automobiles, followed by homes and garages, with the vapor phase concentrations representing more than half of the total BTH (particles + gas). Gas phase concentrations in these environments ranged from 0.2 ppt to 0.3 ppb.[11] Outdoors, BTH in the tens of ppt has been reported,[4,11,13] with levels up to ppb close to sources such as synthetic turf.[4] As a result, assessments of the environmental fates of BTH must include reactions in both the gas and condensed phases as well as indoors and outdoors. This must also include the toxicity of the products, which in most cases, is unknown.[1]

In the atmosphere, hydroxyl (OH) and nitrate ($NO_3$) radicals and ozone are the major gas phase oxidants. Reactions of aromatic molecules with $O_3$ are generally relatively slow, but OH during the day and $NO_3$ at night can be significant removal processes for most organics, including aromatic compounds. The oxidation of aromatic compounds by OH in the gas phase in particular has been extensively studied.[16–20] While there are some experimental studies of oxidation of BTH in the aqueous phase[21–24] in processes involving OH radicals, there are no reports of the gas phase OH–BTH reaction.

We report here the kinetics, products and mechanisms of this reaction in the gas phase using a unique combination of experiment and theory. The results of these two approaches complement and support each other in elucidating atmospheric fates of BTH, including not only the initial attack of OH on BTH but also the subsequent steps involving reactions of molecular oxygen with the OHBTH radical to form stable products.

# 2 Experimental

## 2.1 Kinetics

All experiments were conducted at 1 atm and 298 K under dry conditions. Relative rate studies of the OH oxidation of BTH (TCI, >96.0%) in the gas phase were carried out in a 40 L Teflon chamber (Fig. S1†) using benzene (EMD Chemicals, OmniSolv®) as the reference compound. Benzothiazole vapor was added to the chamber by flowing air (Praxair, Ultra Zero) through the headspace of liquid BTH. Liquid benzene or isopropyl nitrite (IPN, Karl Industries, Ohio) were subjected to two freeze–pump–thaw cycles and a known amount of vapor from the headspace was expanded into an evacuated cell. Benzene and IPN vapor were then flushed into the chamber using Ultra Zero air.

The signal intensities for BTH and benzene were monitored directly in real time by proton-transfer reaction time-of-flight mass spectrometry (PTR-ToF-MS, model 8000, Ionicon Analytik) at a flow rate of 100 $cm^3\ min^{-1}$ and using $H_3O^+$ as the proton source. The concentration of BTH or benzene was then calculated using eqn (A):[25]

$$[M] = \frac{10^9}{k} \cdot \frac{22400 \cdot \mu_0 \cdot U_{\mathrm{drift}}}{N_A \cdot l^2} \cdot \frac{{T_{\mathrm{drift}}}^2}{{T_0}^2} \cdot \frac{{p_0}^2}{{p_{\mathrm{drift}}}^2} \cdot \frac{\mathrm{TR}_{H_3O^+}}{I_{H_3O^+}} \cdot \frac{I_i \cdot \mathrm{Iso}_i}{\mathrm{TR}_i} \quad \text{(A)}$$

In eqn (A), $[M]$ is the concentration of BTH or benzene (ppb); $k$, the reaction rate constant ($2.0 \times 10^{-9}\ cm^3\ s^{-1}$) between $M$ and protonated water reagent ($H_3O^+$); $\mu_0$, the reduced ion mobility, $2.8\ cm^2\ V^{-1}\ s^{-1}$; $U_{\mathrm{drift}}$, the total voltage of the drift tube, 600 V; $N_A$, Avogadro's number; $l$, the length of the reaction chamber, 9.3 cm; $T_{\mathrm{drift}}$, the drift tube temperature, 333 K; $T_0$ and $p_0$, the temperature and pressure under standard conditions, 273.15 K and 1013.25 mbar; $p_{\mathrm{drift}}$, the drift tube pressure (2.2 mbar); $I_i$ and $I_{H_3O^+}$, the signals measured for the ion of interest ($m/z$ 136 for BTH and $m/z$ 79 for benzene) and the $H_3{}^{18}O^+$ ion (taken at $m/z$ 21 with isotopic abundance of 0.002; typical count rate was $\sim 2 \times 10^6\ s^{-1}$), respectively; $TR_i$ and $TR_{H_3O^+}$, are the transmission efficiencies of the ions of interest and the $H_3O^+$ ion respectively; and $Iso_i$, the isotopic abundance of the ion of interest.

The initial concentrations of BTH and benzene in the chamber were 0.4–0.8 ppm and 0.7–1.7 ppm, respectively. Irradiation began when both BTH and benzene intensities at PTRMS were stable (Fig. S2†). Hydroxyl radicals were generated from the photolysis of IPN (2–3 ppm)[26–28] using six blacklights (Sylvania, 350 Blacklight, F15T8/350BL, 15 W):

$$(CH_3)_2CHONO + h\nu\ (\lambda < 450\ \mathrm{nm}) \rightarrow (CH_3)_2CHO^{\bullet} + NO \quad \text{(R1)}$$

$$(CH_3)_2CHO^{\bullet} + O_2 \rightarrow CH_3C(O)CH_3 + HO_2 \quad \text{(R2)}$$

$$HO_2 + NO \rightarrow OH + NO_2 \quad \text{(R3)}$$

## 2.2 Products

For product studies, higher concentrations of BTH (~10–20 ppm) were used to compensate for surface losses, as benzothiazole is a highly adsorptive compound. After the reaction, the contents of the chamber were pumped through a liquid nitrogen trap. The trapped reaction products were dissolved in 50% acetonitrile (Fisher chemical, HPLC grade) and 50% $H_2O$ (Millipore 18.2 mΩ cm) for LC-MS/MS analysis (UPLC-ESI-TQD-MS, Waters and UPLC-HESI-HRMS Orbitrap, Thermo Scientific, Q Exactive Plus). Parameters for both TQD and Orbitrap used in this study were similar to those in previous studies using positive ion mode[28] except that the LC gradients were different. For TQD, the mobile phase was (A) 0.1% formic acid (Fisher Chemical, Optima, LCMS grade) in water and (B) 0.1% formic acid in acetonitrile. The gradient of eluents was 15% B initially, increased to 45% B over 6 min and finally to 95% B over 5 min. It was maintained at 95% B for 2.5 min, and then returned to the initial conditions, where it was held for 3.5 min. For Orbitrap analysis, the mobile phase consisted of (A) 0.1% formic acid in water (Fisher Chemical, Optima) and (B) 0.1% formic acid in

 

acetonitrile. Eluent B was initially set at 5% for 3 min, increased to 95% from 3–14 min, held at 95% for 2 min, and returned to initial conditions linearly over 6 min. Both flow rates were set at 300 μL $min^{-1}$. For MS/MS analysis in the TQD, the collision energy was either 20 or 25 eV.

The following hydroxybenzothiazoles (OHBTHs) and hydroxybenzoic acids (HBAs) were used for product identification (OHBTHs) or testing retention times (HBAs): 2-OHBTH (Thermoscientific, 98%); 4-OHBTH (AA Blocks Inc., 98%); 5-OHBTH (AA Blocks Inc., 95%); 6-OHBTH (AA Blocks Inc., 95%); 7-OHBTH (J & W PharmLab, LLC, 95%); 2HBA (salicylic acid, Fisher Science Education, lab grade); 3HBA (Sigma-Aldrich Co., ReagentPlus®, 99%); and 4HBA (Thermo Scientific, 99+%).

# 3 Theoretical approach

## 3.1 Overview of calculations

The goal of applying theory in this project was to predict the stable reaction products from the reaction of OH radicals with BTH, providing insight into the mechanisms that lead to the experimentally measured products. The calculations were structured to address three main issues. First, the structures of intermediates and products, reaction pathways, and transition states of OH radical attack on BTH were investigated. The intermediate radicals ($n$-OHBTH, where $n = 2, 4, 5, 6, 7$) formed during the initial attack of OH radicals on BTH undergo further reactions with oxygen in the gas phase, leading to the formation of final products. Oxygen, in its ground electronic state, is a triplet electronic state. Thus, the second goal is to consider the role of spin in the reaction, as treating the reactions solely in terms of a single spin state does not adequately capture the complexities involved. A third goal is relating chromatographic retention times with the identity of different products. The hypothesis is that solvation free energy ($\Delta G_{solv}$) is a key parameter determining the sequence in which products elute from a reversed-phase liquid chromatography column and that molecules with more negative solvation-free energies in water will have higher polarity and, consequently, elute earlier.

## 3.2 Spin-state issue

Density Functional Theory (DFT) is a powerful computational tool in quantum chemistry for investigating the electronic structure of molecules, ions, radicals and their reactions.[29–35] While DFT has been successful in studying various reaction mechanisms and optical properties,[36–42] complex open-shell systems can be challenging for DFT and may require the application of more expensive approaches such as the multi-reference method CASPT2 (Complete Active Space Second-Order Perturbation Theory).[43,44] CASPT2, despite its effectiveness, is computationally costly and challenging to apply. Another alternative approach is Constrained Density Functional Theory (CDFT), where spin contamination is explicitly controlled.[45,46] Application of CDFT[47] facilitated addressing the spin issue for systems in a doublet state with an oxygen molecule. The issues encountered with DFT for systems involving $O_2$ molecules are detailed in Text S1 in ESI,† which also presents comparative calculations using both DFT and CDFT to examine the interaction between BTH and the OH radical. These calculations focused on the geometries of pre-reaction complexes, transition states, and post-reaction complexes across five different attack modes. The results demonstrated that CDFT is highly effective for modeling interactions between the OH radical and the BTH molecule. Despite minor discrepancies in energy stabilization, the strong agreement in energy barriers and structural geometries between DFT and CDFT supports the continued use of CDFT for further computational investigations of these reactions.

To determine the transition barrier between the complexes in quartet (three unpaired electrons) and doublet states (one unpaired electron), the potential energy surfaces (PESs) were calculated. These calculations focused on the interaction of $O_2$ with the OHBTH intermediate radical in both states. The energy barrier for the transition from the quartet to the doublet state was identified by analyzing the crossing point of these two curves. Python code was used to calculate the crossing point of the two curves, representing PESs for quartet and doublet states, by interpolating their values using '*interp1d*' from the SciPy library.

## 3.3 Methods

All DFT calculations were performed with the B3LYP hybrid functional[48] and 6-311+G* basis set using the Q-Chem[49] program. It has been previously shown that the B3LYP function provides reasonable results for organic systems in the gas phase and in solution.[29–34] Additionally, the DFT-D3 dispersion corrections from Grimme were applied.[50,51] In this paper, the abbreviation B3LYP-D/6-311+G* is used for this level of theory. The Hessian matrix's negative eigenvalues were examined for all stationary points. Finally, the energy of all stationary points on the PESs was refined by the B2PLYP/6-311++G** method. To address the spin issue in the system with $O_2$, the CDFT approach was used consistently for every molecule and complex. Table S1† lists the charges, multiplicities, and spin constraints for each system used in these calculations.

To predict theoretically the solvation free energy ($\Delta G_{solv}$), the geometries of all five $n$-OHBTH products ($n = 2, 4, 5, 6,$ and 7) were optimized in an aqueous solution using the polarizable continuum model (IEFPCM)[52,53] with the DFT method B3LYP-D/6-311+G*. Solute cavities are constructed from a union of atom-centered spheres whose radii are 1.35 times the atomic van der Waals radii.[33]

# 4 Results and discussion

## 4.1 Experimental results

**4.1.1 Kinetics.** As described elsewhere,[54] the ratio of rate constants for the reactions of OH with BTH ($k_{BTH}$) and ($k_{benzene}$) can be obtained by following the simultaneous decay of BTH and benzene in the Teflon chamber upon irradiation in a mixture of isopropyl nitrite to generate OH:

$$BTH + OH \xrightarrow{k_{BTH}} products \quad (R4)$$

$$\text{Benzene} + \text{OH} \xrightarrow{k_{\text{benzene}}} \text{products} \quad \text{(R5)}$$

$$\ln([\text{BTH}]_0/[\text{BTH}]_t) = (k_{\text{BTH}}/k_{\text{benzene}}) \ln([\text{benzene}]_0/[\text{benzene}]_t) \quad \text{(B)}$$

Fig. 1 shows a plot of typical relative rate data in the form of eqn (B). The relative rate constants measured at 298 K and 1 atm pressure in air are summarized in Table 1. Using a rate constant of $(1.2 \pm 0.15) \times 10^{-12}$ cm$^3$ per molecule per s for the benzene–OH reaction (also at 1 atm and 298 K),[55] the absolute rate constant for the BTH–OH reaction was calculated to be $2.1 \pm 0.3 \times 10^{-12}$ cm$^3$ per molecule per s. The uncertainty is determined largely by that in the rate constant for the reference reaction. The similarity in rate constants for BTH and benzene is reasonable because as discussed below, OH attack on the benzene ring of BTH dominates the reaction. The reported OH–BTH rate constants in the aqueous phase cover a wide range, $(0.95–8.61) \times 10^9$ M$^{-1}$ s$^{-1}$, or in comparable units to those used in the gas phase, $(1.6–14.3) \times 10^{-12}$ cm$^3$ per molecule per s.[21–23] The lower end of the range is similar to the gas phase value measured in the present studies.

Concentrations of the OH radical outdoors typically peak around $10^7$ cm$^{-3}$ at mid-day.[54] Indoors, concentration can reach over $10^6$ molecules per cm$^3$.[56–58] Using our rate constant, the atmospheric lifetime of BTH due to reaction with OH radicals was calculated to be ~13 hours to 5.5 days over these OH concentrations.

**4.1.2 Products.** The OH radical can attack BTH at five different carbon sites, producing hydroxybenzothiazole (OHBTH) isomers that have parent peaks in the mass spectrum at *m*/*z* 152. The exact mass of 152 was confirmed as OHBTH isomers from the Orbitrap analysis. Fig. 2 shows the chromatogram of these products and their assigned structures. The MS/MS spectra of the peaks at different retention times (RT) are shown in Fig. S3.† All OHBTH isomers were confirmed by comparing the retention times (Fig. 2) and their MS/MS fragmentation patterns (Fig. S3†) with those of the standards. Borowska *et al.*[23] reported similar products for the reaction of OH with BTH in aqueous solution, along with some ring-opening products from further oxidation. These products are also consistent with OH oxidation of other aromatic compounds at room temperature, where, for example, phenol is a major product of the OH–benzene reaction.[17,59–62] Relative product yields of each OHBTH are summarized in Table 2. Other than OHBTHs, some nitrobenzothiazoles were also observed (Fig. S4 and S5†). Since IPN was the source of OH radicals, nitrogen dioxide ($NO_2$) was generated in reaction (R3), and its reaction with alkyl radicals can form nitrobenzothiazoles.

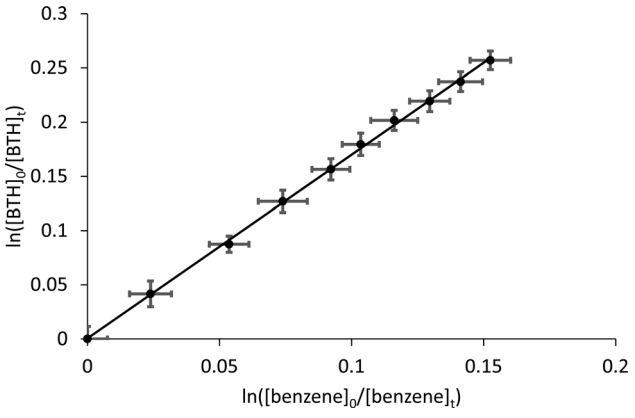


Fig. 1 Typical relative rate data for the reactions of OH radicals with BTH and benzene at 298 K and 1 atm pressure in air.

Table 1 Relative rate constants for the reactions of OH radicals with BTH at 298 K and 1 atm pressure in air using benzene as the reference compound

| Experiments | $[\text{BTH}]_0$ (ppm) | $[\text{Benzene}]_0$ (ppm) | $k_{\text{BTH–OH}}/k_{\text{Benzene–OH}}$ |
|---|---|---|---|
| 1 | 0.5 | 1.2 | 1.93 |
| 2 | 0.8 | 0.7 | 1.83 |
| 3 | 0.6 | 1.7 | 1.71 |
| 4 | 0.4 | 1.6 | 1.71 |
| 5 | 0.6 | 1 | 1.69 |
| 6 | 0.6 | 1.3 | 1.81 |
| 7 | 0.6 | 1.5 | 1.69 |
| | | **Average** | **1.77** |
| | | **1$\sigma$** | **0.09** |

## 4.2 Theoretical results

**4.2.1 Overview.** The attack of hydroxyl radicals (OH) on five distinct carbon atoms (C2, C4, C5, C6, and C7) of the BTH molecule was investigated, revealing a reaction that proceeds through two main steps (Fig. 3). In the first step, the hydroxyl radical adds to the BTH molecule, forming an intermediate radical species, *n*-OHBTH (where $n = 2$, 4, 5, 6, and 7). The existence of the adduct in the case of the OH/benzene reaction has been observed spectroscopically.[63,64] In the second step, the *n*-OHBTH intermediate radical undergoes hydrogen abstraction by $O_2$, forming the final product and a peroxy-radical ($HO_2$). This process involves a spin change in the oxygen molecule, highlighting the complexity and importance of spin dynamics in the reaction mechanism. Theory thus agrees with the experiments in that the presence of $O_2$ is crucial for the oxidation reactions of aromatics in the atmosphere.

This is consistent with studies that have demonstrated that reactions between aromatic molecules such as benzene or 3-methylpyrrole typically occur *via* the initial addition of OH to the aromatic ring: the addition of OH radical is favored over direct H-abstraction in all cases.[42]

The proposed mechanisms for all five reactive sites are shown in Fig. 3. While the initial steps are consistent across all reactions, the reaction involving the C2 carbon atom shows significant differences from C4–7 due to its unique position between the sulfur (S) and nitrogen (N) atoms of the thiazole ring. Thus, the formation of the 2-OHBTH product proceeds through an initially less energetically favorable structure, which then isomerizes to the final product. This additional complexity explains why the OH attack at the BTH on the C2 site involves extra steps in the reaction pathway as detailed below.

 

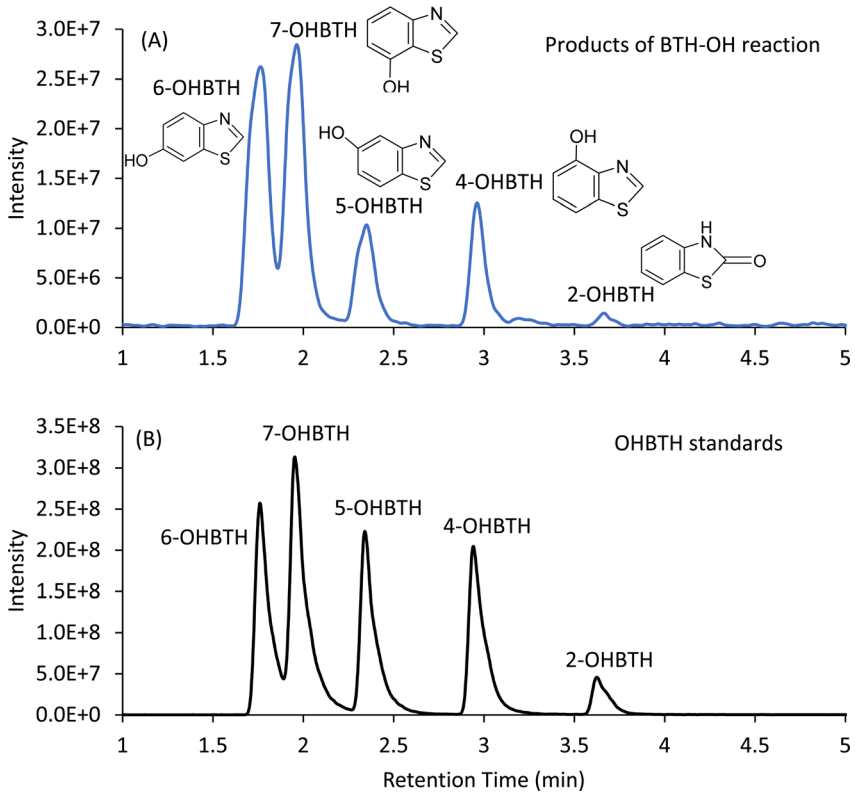


Fig. 2 Extracted ion chromatograms (EIC) of BTH–OH reaction products for *m*/*z* 152 from TQD of (A) products of the reaction of OH with BTH and (B) OHBTH standards (500 ng ml$^{-1}$ each) in 50 : 50 ACN/water.

Table 2 Experimental relative yields of each OHBTH product from the reactions of OH radicals with BTH at 298 K and 1 atm pressure in air, assuming total OHBTH yield is 1

| Experiments | 2-OHBTH | 4-OHBTH | 5-OHBTH | 6-OHBTH | 7-OHBTH |
|---|---|---|---|---|---|
| 1 | 0.06 | 0.14 | 0.13 | 0.30 | 0.37 |
| 2 | 0.07 | 0.23 | 0.09 | 0.27 | 0.34 |
| 3 | 0.07 | 0.15 | 0.14 | 0.37 | 0.27 |
| 4 | 0.06 | 0.15 | 0.11 | 0.30 | 0.38 |
| 5 | 0.05 | 0.08 | 0.19 | 0.38 | 0.30 |
| **Average** | **0.07** | **0.17** | **0.12** | **0.31** | **0.33** |
| **1$\sigma$** | **0.01** | **0.05** | **0.03** | **0.05** | **0.05** |

The C5 pathway is representative of similar reactions at the C4, C6, and C7 positions and thus we focus on the C5 and C2 attack positions to highlight the differences in reaction mechanisms based on the carbon atom's position within the BTH molecule. Detailed treatment of the reactions at sites 4, 6 and 7 is found in the ESI.†

**4.2.2 OH attack on C5 of the benzene ring.** Fig. 4 illustrates the energetics of these reactions and the structures of stationary points on the potential energy surfaces (PESs) for the attack at C5 (see Fig. S6† for the attack at all five positions). This interaction initially forms a stable 5-BTH···OH (**1**) complex with the oxygen atom of the hydroxyl radical coordinated to C5 with distance of 2.42 Å. The H-atom of the hydroxyl radical in this 5-BTH···OH complex (**1**) is oriented toward the benzene ring center. The binding energy is −3.8 kcal mol$^{-1}$ (Table S6†).

Following the reaction coordinate, the 5-BTH···OH system (**1**) passes to the transition state **TS1**, in which the O-atom of hydroxyl radical moves closer to the C5-atom (Fig. 4A and S6†). The activation barrier for the addition of the OH to the BTH molecule is 3.8 kcal mol$^{-1}$ (Fig. 4 and Table S6†) and leads to the formation of stable intermediate radical, 5-OHBTH (**2**), as illustrated in Fig. 4A and B. This process contributes to an additional system stabilization of −12.5 kcal mol$^{-1}$ (Fig. 4A and Table S6†).

The reaction continues when the intermediate radical 5-OHBTH (**2**) interacts with $O_2$ to form a stable 5-OHBTH···$^3O_2$ (**3**) complex with three unpaired electrons (quartet state, Fig. 4A and B). The oxygen molecule is located above the benzene ring of the 5-OHBTH radical, oriented towards the hydrogen atom attached to the carbon center bonded to the OH group. The coordination of $O_2$ to the 5-OHBTH radical additionally stabilizes the system, with a binding energy of 3.6 kcal mol$^{-1}$.

Hydrogen abstraction in the quartet state complex, 5-OHBTH···$^3O_2$, was found not to be energetically favorable. The system energy experiences a significant increase, while the distance decreases between $O_2$ and the H-atom, rising by more than 20 kcal mol$^{-1}$. This substantial energy increase suggests that the reaction pathway involving H-abstraction by $O_2$ in the triplet state may not be a viable route for the formation of the final product. However, if two of the three unpaired electrons in the *n*-OHBTH···$^3O_2$ complex (**3** in Fig. 4A and B) pair up, leaving only one unpaired electron, the complex transitions to a doublet state. In this configuration, the oxygen molecule becomes more

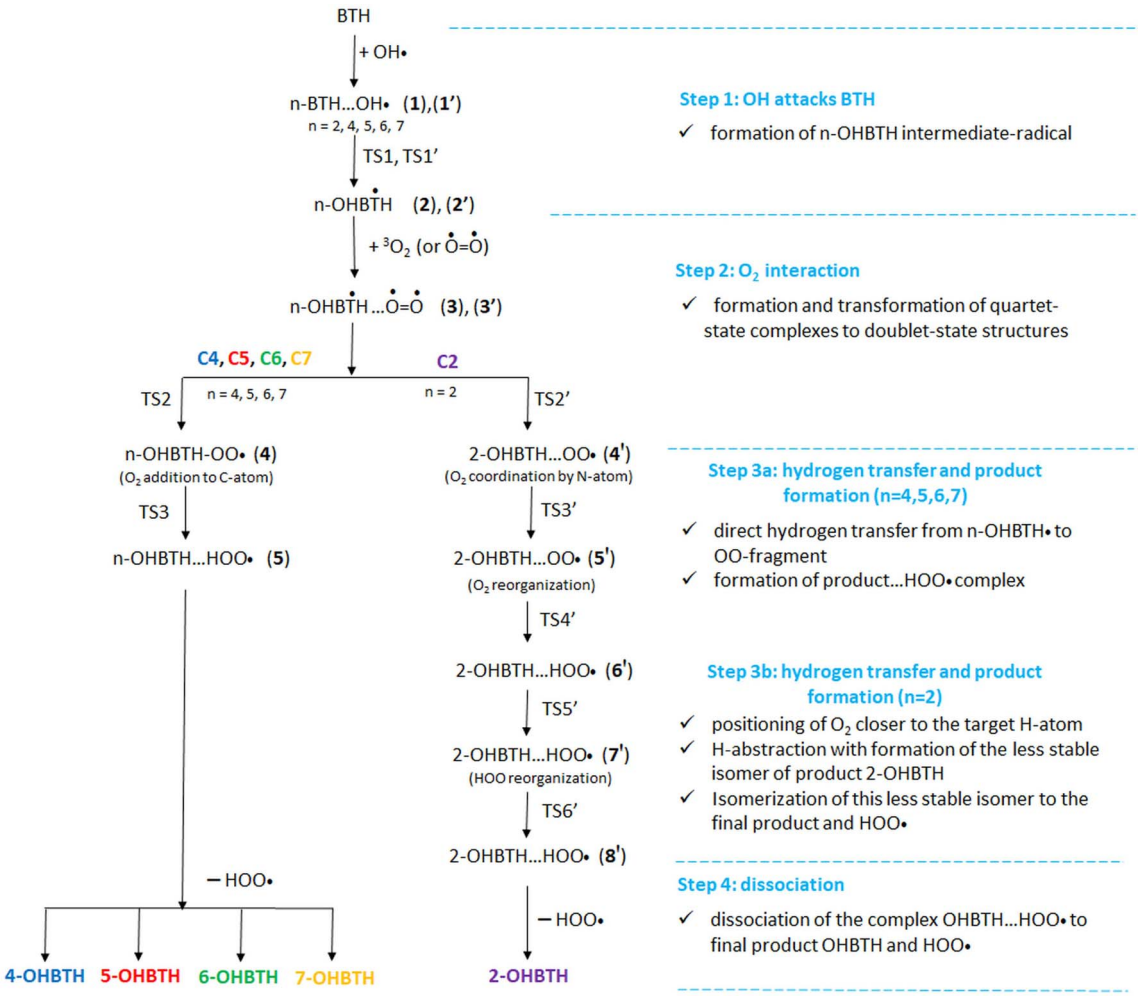


Fig. 3 Proposed mechanism for the reaction of OH with BTH *via* the initial attack on different carbon sites.

reactive, and spontaneously attaches to one of the carbon atoms of the benzene-ring, forming *n*-OHBTH–OO radical (**4** in Fig. 4A and B). Fig. 4B illustrates an example of this sequence of structures for C5-attack. It was found that the preferred sites for $O_2$ addition correspond to the regions of highest spin density values on the 5-OHBTH (**2**) intermediate (Table S8†).

To find the barrier for formation of possible 5-OHBTH–OO intermediates (**4**), the potential energy surfaces (PESs) of the $O_2$ interaction with the 5-OHBTH radical (**2**) were calculated in both states: quartet and doublet. By analyzing the crossing point of these two curves, the approximate energy barrier **TS2** for the system's transition from the quartet to the doublet state was identified: 5-OHBTH$\cdots{}^3O_2$ (**3**) (three unpaired electrons, quartet state) → 5-OHBTH–OO (**4**) (one unpaired electron, doublet state), Fig. S7A.† Only two structures per isomer where the $O_2$ molecule attaches to the carbon atoms adjacent to the carbon with OH group are formed with reasonable barriers (**TS2**). These sites are marked by the green circles in Fig. 5. A crossing between the quartet and doublet curves on the potential energy surfaces (PESs) was not observed for structures where $O_2$ attaches to the carbon atom directly opposite the OH group on the benzene ring, highlighted by red circles in Fig. 5. Therefore, only 5-OHBTH–OO (**4**) structures where $O_2$ is attached to carbon atoms adjacent to the one bonded to the OH group will be considered for subsequent steps of the reaction. These structures are illustrated in Fig. S8.†

Following the reaction pathway, these two 5-OHBTH–OO (**4**) structures evolve into the transition states **TS3**, characterized by the detachment of the OO-fragment from the phenyl ring and its closer approach to the H-atom, accompanied by an elongation of the (C5–H) bond (Fig. 3 and 4). Consequently, the product can follow one of two possible reaction pathways (Table S6†). It was found that for the C5 attack, the pathway with the lowest barriers involves $O_2$ attaching at the C6 site (Fig. 4A and B). This mechanism requires a relatively high barrier of 8.2 kcal mol$^{-1}$ for the $O_2$ addition stage but benefits from a lower barrier of 7.2 kcal mol$^{-1}$ for the subsequent hydrogen abstraction (Table S6†). This comparative analysis underscores the nuanced interplay between stability and reactivity in these chemical systems, highlighting the critical influence of structural and energetic dynamics on the reaction pathways.

**4.2.3 OH attack on C2 in the thiazole ring.** The interaction of OH with BTH also forms a stable 2-BTH$\cdots$OH (**1′**) complex with the oxygen atom of the hydroxyl radical coordinated to the

 

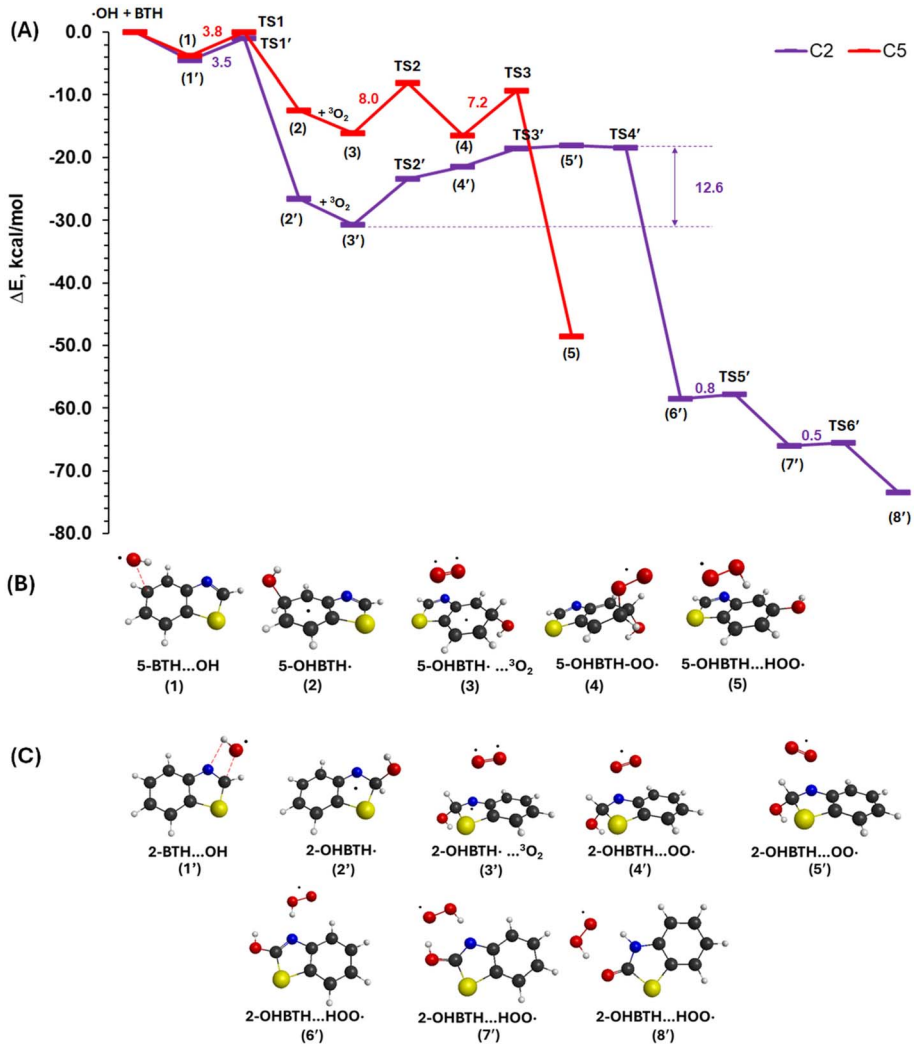


Fig. 4 (A) Stationary points on the PESs of the reaction between BTH and the hydroxyl-radical. The method is (CDFT-B2PLYP/6-311++G**//B3LYP-D/6-311+G*). For the C5 attack, the stationary points are numbered (**1**–**5**), with transition states labeled **TS1**, **TS2**, and **TS3** (in red). The C5 attack scenario also represents cases involving C4, C6, and C7 attacks. For the C2-attack, the stationary points are numbered (**1′**–**8′**) with transition states labeled **TS1′**–**TS6′** (in purple). Note: when zero-point energy corrections are applied in a simple harmonic approximation, the energies of transition states **TS2′**, **TS3′** and **TS4′** become lower than those of the related stationary points. (B) Structures of the stationary points on the PES for the formation of 5-OHBTH. (C) Structures of the stationary points on the PES for the formation of 2-OHBTH. Note: transition state structures can be found in Fig. S9.†

C2 atom and with the hydroxyl H atom oriented to the N3 atom of BTH (formation energy is −4.5 kcal mol$^{-1}$, Table S7†). As shown in Fig. 4A and C, 2-BTH···OH (**1′**) reaches the transition state **TS1** with an activation barrier of 3.5 kcal mol$^{-1}$ and then rearranges to intermediate radical, 2-OHBTH (**2′**) (Table S7†).

The interaction of $O_2$ with the 2-OHBTH radical (**2′**) leads to the formation of the stable 2-OHBTH···$^3O_2$ complex (**3′**) with 3 unpaired electrons and a binding energy close to the other *n*-OHBTH ($n$ = 4, 5, 6, 7) systems, 4.1 kcal mol$^{-1}$ (Fig. 4A, C and Table S7†). In this complex, $O_2$ is positioned above the 2-

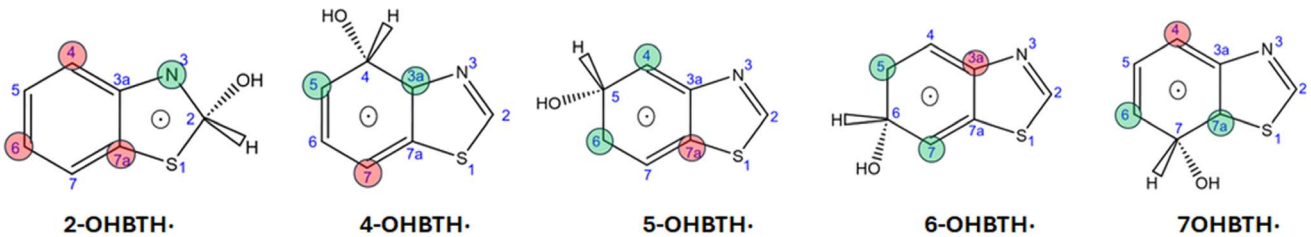


Fig. 5 Oxygen attack sites in the intermediate radical *n*-OHBTH ($n$ = 2, 4, 5, 6,7). The green and red circles highlight the reactive and non-reactive sites of $O_2$ attack, respectively.

OHBTH radical (**2′**) in such a way that one oxygen atom is aligned above the benzene ring. In contrast, the other oxygen atom is situated above the thiazole ring. This second oxygen atom is oriented toward a hydrogen atom, with a distance of 2.86 Å.

In the complex 2-OHBTH$\cdots{}^3O_2$, after one of the unpaired electrons flips its spin, the system converts to the doublet state, and the oxygen attacks the 2-OHBTH radical (**2′**). The electron density distribution analysis in the 2-OHBTH (**2′**) (Table S8†) pinpoints four potential sites for oxygen attachment: N3, C4, C6, and C7a (Fig. 5). Computational calculations of the systems in the doublet state with $O_2$ coordinated at these specific sites leads to formation of two distinct structures for 2-OHBTH–OO, one where the oxygen is bonded to the C6 or C7a sites, and a second one where $O_2$ is coordinated to the N3 atom, structures 2-OHBTH$\cdots$OO (**4′**) in Fig. 4C. The formation of all these doublet state systems leads to an energy rise (Fig. 4A and Table S7†). It was found that only the 2-OHBTH$\cdots$OO complex (**4′**) successfully leads to the final product with reasonable energy barriers (Fig. 4C and S7B†).

The last step, involving hydrogen-abstraction by $O_2$, results in the formation of the 2-OHBTH$\cdots$HOO complex (**8′**). The reaction pathway from 2-OHBTH$\cdots{}^3O_2$ (**3′**) to the final 2-OHBTH$\cdots$HOO (**8′**) proceeds through the transition state **TS2′** and the 2-OHBTH$\cdots$OO complex (**4′**), where $O_2$ is coordinated to the N3 atom, and further involves several subsequent transitions and reorganizations (Fig. 4A and C). Initially, the 2-OHBTH$\cdots$OO complex (**4′**), *via* transition state **TS3′**, reorganizes into 2-OHBTH$\cdots$OO (**5′**), positioning $O_2$ closer (1.96 Å) to the target H-atom. The oxygen abstracts the H-atom (**TS4′**), forming the HOO radical and yielding the 2-OHBTH isomer with the OH group attached to the C2 atom (**6′**). Notably, as the system transitions from (**3′**) to **TS4′**, the energy rises gradually, with a total energy difference of 12.6 kcal mol$^{-1}$ between (**3′**) and (**5′**). A major stabilization occurs when the 2-OHBTH$\cdots$HOO (**6′**) complex is formed, and the energy drops by 40.0 kcal mol$^{-1}$. Subsequently, the product 2-OHBTH in complex (**6′**) isomerizes into a more energetically preferred structure (**8′**) through a hydrogen transfer from the OH group to the N3 atom. This hydrogen transition, facilitated by the $HO_2$ radical, involves two small barriers of less than 1 kcal mol$^{-1}$, related to the re-orientation of $HO_2$ around the 2-OHBTH isomer and the hydrogen transfer itself (Fig. 4A and C).

Thus, the formation of the 2-OHBTH product is a more complex process, requiring more steps and higher energy barriers, than the mechanisms for *n*-OHBTH for $n = 4$, 5, 6, and 7 where OH attacks one of the carbon atoms of the benzene ring. The increased complexity and energy requirement highlight the unique challenges associated with the specific reaction pathways and molecular interactions in the OH-radical/BTH systems.

### 4.3 Experimental and theoretical yields of *n*-OHBTH

Table 2 summarizes the experimentally measured yields for five *n*-OHBTH products ($n = 2$, 4, 5, 6, 7). Based on the average yield, the order of product probability from most to least probable is: 7-OHBTH (33%) > 6-OHBTH (31%) > 4-OHBTH (17%) > 5-OHBTH (12%) > 2-OHBTH (7%).

The Boltzmann distribution was used to calculate the percentage yield and convert these energy differences into probabilities:[65]

$$P_i = \frac{e^{-E_i/RT}}{\sum e^{-E_i/RT}} \cdot 100\% \quad \text{(C)}$$

In eqn (C), $P_i$ is the population of the i-compound in the mixture, $E_i$ is the pre-reaction complex formation energy (Table S6†), $R$ is the gas constant (1.987 cal mol$^{-1}$ K$^{-1}$) and $T$ is the temperature (298 K). Based on eqn (C), the theoretically predicted yields of these four products are approximately 35% for 7-OHBTH, 34% for 6-OHBTH, 17% for 5-OHBTH, and 14% for 4-OHBTH. Thus, the product yields of the OH attack on the benzene ring depend on the formation energy of the pre-reaction complex *n*-BTH$\cdots$OH (1) ($n = 4$, 5, 6, 7). The agreement between experiment and theory is excellent, particularly for 6-OHBTH and 7-OHBTH. While theoretical predictions suggest a higher yield for 5-OHBTH than 4-OHBTH, the experimental results show the reverse. However, given the experimental and theoretical uncertainties, the overall agreement is very good. The agreement with the experimental results supports the equilibrium assumption, which accounts for the effects of collisions that could alter the species distribution following formation reactions. Additionally, when the equilibrium assumption holds, the population distribution becomes independent of reaction barriers. In the case of the OH attack on the C2-atom of the thiazole ring, the pre-reaction complex 2-BTH$\cdots$OH (**1′**) has the lowest formation energy (−4.5 kcal mol$^{-1}$). This suggests that the product 2-OHBTH should have the highest yield compared to other products, such as *n*-OHBTH ($n = 4$, 5, 6, 7). However, as discussed above, forming the 2-OHBTH is a more complex process, requiring additional steps and higher energy barriers than the mechanisms involved in forming the other products from the attack on the benzene ring. This increased complexity and higher energy requirement are consistent with the experimentally observed smaller yield of the 2-OHBTH product (Table 2).

Rate calculations, such as Rice–Ramsperger–Kassel–Marcus (RRKM) theory or Transition State Theory (TST), as well as higher-level methods, demand significant computational effort on potential energy surfaces, which extends beyond the scope of this project. Nevertheless, potential energy barriers offer valuable, albeit semi-quantitative, insights into the reaction mechanisms and we hope to calculate the rate using the necessary input on the potential energy surfaces in the future.

### 4.4 Predicting chromatographic elution order using solvation energy principles

The elution order of products 6-OHBTH, 7-OHBTH, 5-OHBTH, 4-OHBTH, and 2-OHBTH was determined experimentally by measuring the retention times of standard samples of these compounds (Fig. 2). The retention time of these products was predicted theoretically as well. The theoretical approach is based on the assumption that solvation free energy ($\Delta G_{solv}$) is

 

a key parameter determining the sequence in which products elute from a reversed-phase liquid chromatography column. This principle leverages the relationship between polarity and elution order in liquid chromatography, where more polar molecules typically elute first. The hypothesis posits that molecules with more negative solvation energies in water will have higher polarity and, consequently, elute earlier through the column.

To test this, the retention times of three isomers of hydroxybenzoic acid—4HBA, 3HBA and 2HBA—were first experimentally determined (Fig. S10A†). These HBA measurements were necessary for theoretical calculations, as they provided additional reference data for compounds with similar structures, helping to validate our retention time prediction model. Theory accurately predicted the elution order for the hydroxybenzoic acids: 4HBA, followed by 3HBA, and then 2HBA (Fig. S11A†). However, for the *n*-OHBTH systems, 2-OHBTH has the lowest $\Delta G_{solv}$, which would place it at the beginning of the elution sequence, even though it was last in this series experimentally (Fig. S10A†).

The isomer 2-OHBTH was shown to form a dimer with a formation energy of $-14$ kcal mol$^{-1}$. Calculations for the dimer improved the performance of the model, but still predicted that the dimer should elute before the 4-OHBTH isomer (Fig. S11A†). Another issue relates to the structure of 4-OHBTH, which, according to experimental data, should appear fourth in the sequence, just before 2-OHBTH. In the present calculations, its highest $\Delta G_{solv}$ value incorrectly places it at the end (Fig. S11A†).

Comparison of the theoretically predicted $\Delta G_{solv}$ values for systems HBA and OHBTH with the experiment indicates that the $\Delta G_{solv}$ of both 2HBA and 4-OHBTH are overestimated. This can be related to the internal hydrogen bonds formed by the hydroxy-group in these molecules, making the pure IEFPCM model insufficient to capture all solvent effects (Fig. S11B†). To address this, the inclusion of external water molecules, which are present in the mobile phase of the eluting solvent, together with IEFPCM may be required. However, overall, there is reasonable agreement between theoretical predictions and experimental results, demonstrating a relationship between solvation-free energy and elution order in liquid chromatography. This makes $\Delta G_{solv}$ a useful parameter to help predict elution order, though with some caution.

## 5 Summary and conclusions

The reaction of OH with BTH is sufficiently fast ($k = 2.1 \pm 0.3$ ($1\sigma$) $\times$ $10^{-12}$ cm$^3$ per molecule per s) that the estimated lifetimes of BTH in air range from about 13 hours to 5.5 days over OH concentrations of $10^7$–$10^6$ cm$^{-3}$. Thus, this reaction represents a significant loss process for BTH in air both outdoors and indoors, and exposures and toxicity of both the parent BTH and its oxidation products need to be taken into account.

Experiment and theory of the products of the gas phase reaction of OH radicals with BTH are in excellent agreement overall. The reaction occurs in two main steps: the addition of the OH radical to BTH, followed by what is, in effect, a hydrogen abstraction by $O_2$ to give the final OHBTH products and $HO_2$ radical. The complex formed by the *n*-OHBTH intermediate radical with $O_2$ results in an *n*-OHBTH$\cdots{}^3O_2$ system with three unpaired electrons. However, for the reaction to continue, one of the electrons must flip its spin to pair with another electron, allowing the system to transition to a double state with a single unpaired electron.

Significant differences were identified in the mechanisms underlying product formation for attack on the benzene ring compared to attack on the thiazole ring. In the first case, the yields of products 4-OHBTH, 5-OHBTH, 6-OHBTH and 7-OHBTH are consistent with theory predictions based on energies of formation of the pre-reaction OH$\cdots$BTH complex. However, in the case of attack on C2 of the thiazole ring, $O_2$ coordinates to the N3 atom without bonding, unlike the first case where it adds to the carbon near the OH group. Additionally, 2-OHBTH formation involves higher energy barriers and extra steps for reorganization and isomerization. These differences are due to the unique position of the C2 atom between the N and S atoms.

The relationships predicted between chromatographic retention times and free solvation energies ($\Delta G_{solv}$) are in reasonable agreement with experimental data obtained using standards for hydroxybenzoic acids: 4HBA (1st), 3HBA (2nd), and 2HBA (3rd). In the case of *n*-OHBTH where $n = 2$, 4, 5, 6, 7, the relative positions of $n = 2$, 5, 6 and 7 agree with the experiment, but that of 4-OHBTH is incorrect. The free solvation energies of molecules with internal hydrogen bonds, such as 4-OHBTH and 2HBA, may be overestimated using the IEFPCM model.

The combination of experiment and theory used here to understand BTH oxidation by OH radicals can be applied more broadly to derivatives of BTH, and other emerging contaminants, illustrating the power of this combination in addressing the environmental fates of compounds for which there are few data.

## Data availability

All relevant data are included in the text and ESI.†

## Conflicts of interest

There are no conflicts to declare.

## Acknowledgements

The authors thank Dr Imon Mandal for her helpful comments and discussions. We are grateful to the National Science Foundation (#2303948) for supporting this work. RBG was also supported by the Israel Science Foundation, grant 593/20. Additionally, the authors would like to thank SDSC for the Advanced Cyberinfrastructure Coordination Ecosystem: Services & Support (ACCESS) program,[66] which is supported by National Science Foundation grants TG-EES240032.

## References

1 C. Liao, U.-J. Kim and K. Kannan, A Review of Environmental Occurrence, Fate, Exposure, and Toxicity of Benzothiazoles, *Environ. Sci. Technol.*, 2018, **52**, 5007–5026.
2 M. Celeiro, D. Armada, T. Dagnac, J. de Boer and M. Llompart, Hazardous Compounds in Recreational and Urban Recycled Surfaces Made from Crumb Rubber. Compliance with Current Regulation and Future Perspectives, *Sci. Total Environ.*, 2021, **755**, 142566.
3 G. Ginsberg, B. Toal, N. Simcox, A. Bracker, B. Golembiewski, T. Kurland and C. Hedman, Health Risk Assessment of Synthetic Turf Fields Based upon Investigation of Five Fields in Connecticut, *J. Toxicol. Environ. Health, Part A*, 2011, **74**, 1150–1174.
4 N. J. Simcox, A. Bracker, G. Ginsberg, B. Toal, B. Golembiewski, T. Kurland and C. Hedman, Synthetic Turf Field Investigation in Connecticut, *J. Toxicol. Environ. Health, Part A*, 2011, **74**, 1133–1149.
5 X. Li, W. Berger, C. Musante and M. I. Mattina, Characterization of Substances Released from Crumb Rubber Material Used on Artificial Turf Fields, *Chemosphere*, 2010, **80**, 279–285.
6 I. Schmeltz and D. Hoffmann, Nitrogen-Containing Compounds in Tobacco and Tobacco-Smoke, *Chem. Rev.*, 1977, **77**, 295–311.
7 F. Iadaresta, M. D. Manniello, C. Ostman, C. Crescenzi, J. Holmback and P. Russo, Chemicals from Textiles to Skin: An in Vitro Permeation Study of Benzothiazole, *Environ. Sci. Pollut. Res.*, 2018, **25**, 24629–24638.
8 D. Garcia-Gomez, L. Bregy, Y. Nussbaumer-Ochsner, T. Gaisl, M. Kohler and R. Zenobi, Detection and Quantification of Benzothiazoles in Exhaled Breath and Exhaled Breath Condensate by Real-Time Secondary Electrospray Ionization-High-Resolution Mass Spectrometry and Ultra-High Performance Liquid Chromatography, *Environ. Sci. Technol.*, 2015, **49**, 12519–12524.
9 Y.-J. Li and W.-H. Ding, Determination of Benzotriazole and Benzothiazole Derivatives in Human Urine by Eco-Friendly Deep Eutectic Solvent-Based Ultrasound-Assisted Liquid-Liquid Microextraction Followed by Ultrahigh Performance Liquid Chromatography Quadrupole-Time-of-Flight Mass Spectrometry, *Environ. Pollut.*, 2021, **284**, 17530.
10 Z. Tkalec, A. A. Runkel, T. Kosjek, M. Horvat and E. Heath, Contaminants of Emerging Concern in Urine: A Review of Analytical Methods for Determining Diisocyanates, Benzotriazoles, Benzothiazoles, 4-Methylbenzylidene Camphor, Isothiazolinones, Fragrances, and Non-Phthalate Plasticizers, *Environ. Sci. Pollut. Res.*, 2023, **30**, 95106–95138.
11 Y. Wan, J. Xue and K. Kannan, Benzothiazoles in Indoor Air from Albany, New York, USA, and Its Implications for Inhalation Exposure, *J. Hazard. Mater.*, 2016, **311**, 37–42.
12 A. Maceira, R. Maria Marce and F. Borrull, Occurrence of Benzothiazole, Benzotriazole and Benzenesulfonamide Derivates in Outdoor Air Particulate Matter Samples and Human Exposure Assessment, *Chemosphere*, 2018, **193**, 557–566.
13 E. B. Franklin, M. R. Alves, A. N. Moore, D. B. Kilgour, G. A. Novak, K. Mayer, J. S. Sauer, R. J. Weber, D. Dang, M. Winter, C. Lee, C. D. Cappa, T. H. Bertram, K. A. Prather, V. H. Grassian and A. H. Goldstein, Atmospheric Benzothiazoles in a Coastal Marine Environment, *Environ. Sci. Technol.*, 2021, **55**, 15705–15714.
14 C. Deng, J. Huang, Y. Qi, D. Chen and W. Huang, Distribution Patterns of Rubber Tire-Related Chemicals with Particle Size in Road and Indoor Parking Lot Dust, *Sci. Total Environ.*, 2022, **844**, 157144.
15 M. Feltracco, G. Mazzi, E. Barbaro, E. Gregoris, M. Bortolini, C. Barbante and A. Gambaro, Insights into Size-Segregated Distribution of Benzothiazoles in Indoor Aerosol from Office Environments, *Environ. Sci.: Atmos.*, 2024, **4**, 571–577.
16 R. Atkinson and J. Arey, Atmospheric Degradation of Volatile Organic Compounds, *Chem. Rev.*, 2003, **103**, 4605–4638.
17 K. H. Bates, D. J. Jacob, K. Li, P. D. Ivatt, M. J. Evans, Y. Y. Yan and J. T. Lin, Development and Evaluation of a New Compact Mechanism for Aromatic Oxidation in Atmospheric Models, *Atmos. Chem. Phys.*, 2021, **21**, 18351–18374.
18 W. P. L. Carter and G. Heo, Development of Revised SAPRC Aromatics Mechanisms, *Atmos. Environ.*, 2013, **77**, 404–414.
19 L. Vereecken, in *Advances in Atmospheric Chemistry*, ed. J. R. Barker, A. L. Steiner and T. W. Wallington, World Scientific Publishing, 2019, ch. 6, vol. 2, pp. 377–527.
20 Z. Yang, L. Du, Y. Li and X. Ge, Secondary Organic Aerosol Formation from Monocyclic Aromatic Hydrocarbons: Insights from Laboratory Studies, *Environ. Sci.: Processes Impacts*, 2022, **24**, 351–379.
21 R. Andreozzi, V. Caprio and R. Marotta, Oxidation of Benzothiazole, 2-Mercaptobenzothiazole and 2-Hydroxybenzothiazole in Aqueous Solution by Means of $H_2O_2$/UV or Photoassisted Fenton Systems, *J. Chem. Technol. Biotechnol.*, 2001, **76**, 196–202.
22 S. Bahnmüller, C. H. Loi, K. L. Linge, U. V. Gunten and S. Canonica, Degradation Rates of Benzotriazoles and Benzothiazoles Under UV-C Irradiation and the Advanced Oxidation Process UV/$H_2O_2$, *Water Res.*, 2015, **74**, 143–154.
23 E. Borowska, E. Felis and J. Kalka, Oxidation of Benzotriazole and Benzothiazole in Photochemical Processes: Kinetics and Formation of Transformation Products, *Chem. Eng. J.*, 2016, **304**, 852–863.
24 X. Han, X. Zhang, L. Zhang, M. Pan and J. Yan, Benzothiazole Heterogeneous Photodegradation in Nano α-$Fe_2O_3$/Oxalate System Under UV Light Irradiation, *R. Soc. Open Sci.*, 2018, **5**, 180322.
25 V. Perraud, S. Meinardi, D. R. Blake and B. J. Finlayson-Pitts, Challenges Associated with the Sampling and Analysis of Organosulfur Compounds in Air Using Real-Time PTR-ToF-MS and Offline GC-FID, *Atmos. Meas. Tech.*, 2016, **9**, 1325–1340.
26 B. J. Finlayson-Pitts, A. Anderson, P. S. J. Lakey, W. Wang, M. J. Ezell, X. Wang, L. M. Wingen, V. Perraud and M. Shiraiwa, Oxidation of Solid Thin Films of

 

Neonicotinoid Pesticides by Gas Phase Hydroxyl Radicals, *Environ. Sci.: Atmos.*, 2023, **3**, 124–142.

27 J. D. Raff and B. J. Finlayson-Pitts, Hydroxyl Radical Quantum Yields from Isopropyl Nitrite Photolysis in Air, *Environ. Sci. Technol.*, 2010, **44**, 8150–8155.

28 X. Wang, W. Wang, L. M. Wingen, V. Perraud and B. J. Finlayson-Pitts, Top–Down Versus Bottom–Up Oxidation of a Neonicotinoid Pesticide by OH Radicals, *Proc. Natl. Acad. Sci. U.S.A.*, 2024, **121**, e2312930121.

29 N. V. Karimova, J. Chen, J. R. Gord, S. Staudt, T. H. Bertram, G. M. Nathanson and R. B. Gerber, SN2 Reactions of N2O5 with Ions in Water: Microscopic Mechanisms, Intermediates, and Products, *J. Phys. Chem. A*, 2020, **124**, 711–720.

30 N. V. Karimova, M. Luo, I. Sit, V. H. Grassian and R. B. Gerber, Absorption Spectra and the Electronic Structure of Gallic Acid in Water at Different pH: Experimental Data and Theoretical Cluster Models, *J. Phys. Chem. A*, 2022, **126**, 190–197.

31 N. V. Karimova, L. M. McCaslin and R. B. Gerber, Ion Reactions in Atmospherically-Relevant Clusters: Mechanisms, Dynamics and Spectroscopic Signatures, *Faraday Discuss.*, 2019, **217**, 342–360.

32 S. Staudt, J. R. Gord, N. V. Karimova, E. E. McDuffie, S. S. Brown, R. B. Gerber, G. M. Nathanson and T. H. Bertram, Sulfate and Carboxylate Suppress the Formation of $ClNO_2$ at Atmospheric Interfaces, *ACS Earth Space Chem.*, 2019, **3**, 1987–1997.

33 N. M. Vitkovskaya, E. Y. Larionova, V. B. Kobychev, N. V. Kaempf and B. A. Trofimov, A Theoretical Study of Methanol Vinylation Reaction Mechanism, *Int. J. Quantum Chem.*, 2008, **108**, 2630–2635.

34 N. M. Vitkovskaya, E. Y. Larionova, V. B. Kobychev, N. V. Kaempf and B. A. Trofimov, Methanol Vinylation Mechanism in the KOH/DMSO/$CH_3OH$/$C_2H_2$ System, *Int. J. Quantum Chem.*, 2011, **111**, 2519–2524.

35 B. Tang, Q. Bai, Y.-G. Fang, J. S. Francisco, C. Zhu and W.-H. Fang, Mechanistic Insights into N2O5-Halide Ions Chemistry at the Air–Water Interface, *J. Am. Chem. Soc.*, 2024, 21742–21751.

36 J. R. Church, V. Vaida and R. T. Skodje, Gas-Phase Reaction Kinetics of Pyruvic Acid with OH Radicals: The Role of Tunneling, Complex Formation, and Conformational Structure, *J. Phys. Chem. A*, 2020, **124**, 790–800.

37 C. D. Daub, I. Zakai, R. Valiev, V.-T. Salo, R. B. Gerber and T. Kurtén, Energy Transfer, Pre-Reactive Complex Formation and Recombination Reactions During the Collision of Peroxy Radicals, *Phys. Chem. Chem. Phys.*, 2022, **24**, 10033–10043.

38 A. Fernando and C. M. Aikens, Reaction Pathways for Water Oxidation to Molecular Oxygen Mediated by Model Cobalt Oxide Dimer and Cubane Catalysts, *J. Phys. Chem. A*, 2015, **119**, 11072–11085.

39 J. I. Mujika, J. Uranga and J. M. Matxain, Computational Study on the Attack of OH Radicals on Aromatic Amino Acids, *Chem.–Eur. J.*, 2013, **19**, 6862–6873.

40 I. Nikšić-Franjić and I. Ljubić, Comparing the Performances of Various Density Functionals for Modelling the Mechanisms and Kinetics of Bimolecular Free Radical Reactions in Aqueous Solution, *Phys. Chem. Chem. Phys.*, 2019, **21**, 23425–23440.

41 A. M. Priya and S. Lakshmipathi, DFT Study on Abstraction Reaction Mechanism of OH Radical with 2-Methoxyphenol, *J. Phys. Org. Chem.*, 2017, **30**, e3713.

42 G. P. F. Wood, A. Sreedhara, J. M. Moore and B. L. Trout, Reactions of Benzene and 3-Methylpyrrole with the $^{\bullet}OH$ and $^{\bullet}OOH$ Radicals: An Assessment of Contemporary Density Functional Theory Methods, *J. Phys. Chem. A*, 2014, **118**, 2667–2682.

43 K. Andersson, P.-Å. Malmqvist and B. O. Roos, Second-Order Perturbation Theory with a Complete Active Space Self-Consistent Field Reference Function, *J. Chem. Phys.*, 1992, **96**, 1218–1226.

44 G. Hasan, V.-T. Salo, R. R. Valiev, J. Kubečka and T. Kurtén, Comparing Reaction Routes for 3(RO$\cdots$OR') Intermediates Formed in Peroxy Radical Self- and Cross-Reactions, *J. Phys. Chem. A*, 2020, **124**, 8305–8320.

45 J. R. Schmidt, N. Shenvi and J. C. Tully, Controlling Spin Contamination Using Constrained Density Functional Theory, *J. Chem. Phys.*, 2008, **129**, 114110.

46 M. E. Varner, M. E. Harding, J. Gauss and J. F. Stanton, On the Geometry of the $HO_3$ Radical, *J. Chem. Phys.*, 2008, **346**, 53–55.

47 Q. Wu and T. Van Voorhis, Direct Optimization Method to Study Constrained Systems within Density-Functional Theory, *Phys. Rev. A*, 2005, **72**, 024502.

48 P. J. Stephens, F. J. Devlin, C. F. Chabalowski and M. J. Frisch, Ab Initio Calculation of Vibrational Absorption and Circular Dichroism Spectra Using Density Functional Force Fields, *J. Phys. Chem. A*, 1994, **98**, 11623–11627.

49 Y. Shao, Z. Gan, E. Epifanovsky, A. T. B. Gilbert, M. Wormit, J. Kussmann, A. W. Lange, A. Behn, J. Deng, X. Feng, D. Ghosh, M. Goldey, P. R. Horn, L. D. Jacobson, I. Kaliman, R. Z. Khaliullin, T. Kuś, A. Landau, J. Liu, E. I. Proynov, Y. M. Rhee, R. M. Richard, M. A. Rohrdanz, R. P. Steele, E. J. Sundstrom, H. L. Woodcock, P. M. Zimmerman, D. Zuev, B. Albrecht, E. Alguire, B. Austin, G. J. O. Beran, Y. A. Bernard, E. Berquist, K. Brandhorst, K. B. Bravaya, S. T. Brown, D. Casanova, C.-M. Chang, Y. Chen, S. H. Chien, K. D. Closser, D. L. Crittenden, M. Diedenhofen, R. A. DiStasio, H. Do, A. D. Dutoi, R. G. Edgar, S. Fatehi, L. Fusti-Molnar, A. Ghysels, A. Golubeva-Zadorozhnaya, J. Gomes, M. W. D. Hanson-Heine, P. H. P. Harbach, A. W. Hauser, E. G. Hohenstein, Z. C. Holden, T.-C. Jagau, H. Ji, B. Kaduk, K. Khistyaev, J. Kim, J. Kim, R. A. King, P. Klunzinger, D. Kosenkov, T. Kowalczyk, C. M. Krauter, K. U. Lao, A. D. Laurent, K. V. Lawler, S. V. Levchenko, C. Y. Lin, F. Liu, E. Livshits, R. C. Lochan, A. Luenser, P. Manohar, S. F. Manzer, S.-P. Mao, N. Mardirossian, A. V. Marenich, S. A. Maurer, N. J. Mayhall, E. Neuscamman, C. M. Oana, R. Olivares-Amaya,

D. P. O'Neill, J. A. Parkhill, T. M. Perrine, R. Peverati, A. Prociuk, D. R. Rehn, E. Rosta, N. J. Russ, S. M. Sharada, S. Sharma, D. W. Small, A. Sodt, T. Stein, D. Stück, Y.-C. Su, A. J. W. Thom, T. Tsuchimochi, V. Vanovschi, L. Vogt, O. Vydrov, T. Wang, M. A. Watson, J. Wenzel, A. White, C. F. Williams, J. Yang, S. Yeganeh, S. R. Yost, Z.-Q. You, I. Y. Zhang, X. Zhang, Y. Zhao, B. R. Brooks, G. K. L. Chan, D. M. Chipman, C. J. Cramer, W. A. Goddard, M. S. Gordon, W. J. Hehre, A. Klamt, H. F. Schaefer, M. W. Schmidt, C. D. Sherrill, D. G. Truhlar, A. Warshel, X. Xu, A. Aspuru-Guzik, R. Baer, A. T. Bell, N. A. Besley, J.-D. Chai, A. Dreuw, B. D. Dunietz, T. R. Furlani, S. R. Gwaltney, C.-P. Hsu, Y. Jung, J. Kong, D. S. Lambrecht, W. Liang, C. Ochsenfeld, V. A. Rassolov, L. V. Slipchenko, J. E. Subotnik, T. Van Voorhis, J. M. Herbert, A. I. Krylov, P. M. W. Gill and M. Head-Gordon, Advances in Molecular Quantum Chemistry Contained in the Q-Chem 4 Program Package, *Mol. Phys.*, 2015, **113**, 184–215.

50 S. Grimme, Semiempirical GGA-Type Density Functional Constructed with a Long-Range Dispersion Correction, *J. Comput. Chem.*, 2006, **27**, 1787–1799.

51 S. Grimme, J. Antony, S. Ehrlich and H. Krieg, A Consistent and Accurate Ab Initio Parametrization of Density Functional Dispersion Correction (DFT-D) for the 94 Elements H-Pu, *J. Chem. Phys.*, 2010, **132**, 154104.

52 M. Caricato, B. Mennucci, J. Tomasi, F. Ingrosso, R. Cammi, S. Corni and G. Scalmani, Formation and Relaxation of Excited States in Solution: A New Time Dependent Polarizable Continuum Model Based on Time Dependent Density Functional Theory, *J. Chem. Phys.*, 2006, **124**, 124520.

53 D. M. Chipman, Comparison of Solvent Reaction Field Representations, *Theor. Chem. Accounts Theor. Comput. Model.*, 2002, **107**, 80–89.

54 B. J. Finlayson-Pitts and J. N. Pitts, *Chemistry of the Upper and Lower Atmosphere: Theory, Experiments, and Applications*, Academic Press, 2000.

55 A. Mellouki, M. Ammann, R. A. Cox, J. N. Crowley, H. Herrmann, M. E. Jenkin, V. F. McNeill, J. Troe and T. J. Wallington, Evaluated kinetic and photochemical data for atmospheric chemistry: volume VIII - gas-phase reactions of organic species with four, or more, carbon atoms ($\geq C_4$), *Atmos. Chem. Phys.*, 2021, **21**, 4797–4808.

56 E. GomezAlvarez, D. Amedro, C. Afif, S. Gligorovski, C. Schoemaecker, C. Fittschen, J. F. Doussin and H. Wortham, Unexpectedly high indoor hydroxyl radical concentrations associated with nitrous acid, *Proc. Natl. Acad. Sci. U.S.A.*, 2013, **110**, 13294–13299.

57 J. P. Liu, S. Li, J. F. Zeng, M. Mekic, Z. J. Yu, W. T. Zhou, G. Loisel, A. Gandolfo, W. Song, X. M. Wang, Z. Zhou, H. Herrmann, X. Li and S. Gligorovski, Assessing indoor gas phase oxidation capacity through real-time measurements of HONO and $NO_x$ in Guangzhou, China, *Environ. Sci.: Processes Impacts*, 2019, **21**, 1393–1402.

58 E. Reidy, B. P. Bottorff, C. M. F. Rosales, F. J. Cardoso-Saldaña, C. Arata, S. Zhou, C. Wang, A. Abeleira, L. Hildebrandt Ruiz, A. H. Goldstein, A. Novoselac, T. F. Kahan, J. P. D. Abbatt, M. E. Vance, D. K. Farmer and P. S. Stevens, Measurements of Hydroxyl Radical Concentrations during Indoor Cooking Events: Evidence of an Unmeasured Photolytic Source of Radicals, *Environ. Sci. Technol.*, 2023, **57**, 896–908.

59 R. Atkinson and J. Arey, Mechanisms of the Gas-Phase Reactions of Aromatic Hydrocarbons and PAHS with OH and $NO_3$ Radicals, *Polycyclic Aromat. Compd.*, 2007, **27**, 15–40.

60 T. Berndt and O. Böge, Gas-Phase Reaction of OH Radicals with Benzene: Products and Mechanism, *Phys. Chem. Chem. Phys.*, 2001, **3**, 4946–4956.

61 T. Berndt and O. Böge, Formation of Phenol and Carbonyls from the Atmospheric Reaction of OH Radicals with Benzene, *Phys. Chem. Chem. Phys.*, 2006, **8**, 1205.

62 R. Volkamer, B. Klotz, I. Barnes, T. Imamura, K. Wirtz, N. Washida, K. H. Becker and U. Platt, OH-Initiated Oxidation of Benzene - Part I. Phenol Formation under Atmospheric Conditions, *Phys. Chem. Chem. Phys.*, 2002, **4**, 1598–1610.

63 R. Knispel, R. Koch, M. Siese and C. Zetzsch, Adduct Formation of OH Radicals with Benzene, Toluene, and Phenol and Consecutive Reactions of the Adducts with $NO_x$ and $O_2$, *Ber. Bunsenges. Phys. Chem.*, 1990, **94**, 1375–1379.

64 B. Fritz, V. Handwerk, M. Preidel and R. Zellner, Direct Detection of Hydroxy-Cyclohexadienyl in the Gas Phase by cw-UV-Laser Absorption, *Ber. Bunsenges. Phys. Chem.*, 1985, **89**, 343–344.

65 T. L. Hill, *An Introduction to Statistical Thermodynamics*, Addison-Wesley Publishing Company, USA, 1960.

66 T. J. Boerner, S. Deems, T. R. Furlani, S. L. Knuth and J. Towns, *Presented in Part at the Practice and Experience in Advanced Research Computing*, Portland, OR, USA, 2023.

 